An Open-Source Hierarchical Multi-fidelity Modeling Stack for Design and Analysis of Compliant Mechanisms

Hai-Jun Su[1]
Department of Mechanical & Aerospace Engineering,
The Ohio State University,
Columbus, Ohio, USA
email: su.298@osu.edu

Benjamin Servey
Department of Mechanical & Aerospace Engineering,
The Ohio State University,
Columbus, Ohio, USA

This paper presents an open-source, hierarchical, eight-level multi-fidelity modeling stack as a comprehensive technical routine for the design and analysis of compliant mechanisms, utilizing the widely adopted parallelogram flexure as a representative case study. Our methodology involves the systematic implementation, integration, and cross-validation of modeling levels spanning from first-order linear beam theories and refined pseudo-rigid-body models (PRBM) with optimized characteristic radius factors, to intermediate beam constraint models (BCM), exact transcendental solutions for fixed-guided beams, numerical boundary value problem (BVP) systems, and high-fidelity 3-D solid finite element analysis (FEA). All solvers, benchmarking datasets, and interactive tools have been developed as an open-source contribution to facilitate community adoption and further research. Major results demonstrate an excellent performance spread of over eight orders of magnitude in computational runtime, ranging from sub-microsecond algebraic evaluations to solid-mesh simulations requiring nearly a minute per load case. Furthermore, we quantify the localized divergence of low-fidelity models in predicting critical second-order effects, such as parasitic rotations and nonlinear softening/stiffening behavior near buckling thresholds. Based on the summary of these benchmark test results, a practical model selection guide is concluded to assist designers in selecting optimal modeling fidelities for various flexure systems, facilitating the rapid synthesis of precision mechanisms with guaranteed accuracy across expansive workspaces.

Keywords: compliant mechanisms, multi-fidelity modeling, beam constraint model, pseudo-rigid-body model, finite element analysis, large deflections

1 Introduction

Compliant mechanisms (CMs) represent a significant departure from traditional rigid-body kinematics, achieving motion through the elastic deformation of flexible members rather than solely via discrete kinematic pairs [1]. Inspired by the pervasive compliance found in biological systems, these mechanisms offer transformative advantages for high-performance engineering, including the elimination of backlash and friction, reduced part count, and the capability for extreme miniaturization. Consequently, CMs have become indispensable in precision application domains such as nanomanufacturing, optical manipulation stages, and surgico-robotic instruments where traditional joints would introduce impermissible positioning and repeatability errors [2,3].

Despite their advantages, the design and analysis of CMs remain fraught with fundamental challenges that constitute major "open problems" in the field. A primary difficulty is the deep coupling between kinematics and elastomechanics; unlike rigid-body systems where geometry and force can be decoupled, the motion of a CM is an intrinsic function of its instantaneous loading state and material properties. Furthermore, these mechanisms often operate in large-deflection regimes where geometric nonlinearities—such as elastokinematic shortening, load-stiffening, and buckling—dominate behavior. Bridging the gap between conceptual synthesis and high-fidelity physical validation remains a significant hurdle for designers, often resulting in costly prototyping iterations due to a lack of integrated modeling frameworks.

The current state-of-the-art in reduced-order modeling for planar flexures generally spans a spectrum of fidelities, ranging from linear beam theory to exact analytical solutions. Linear beam theory provides a rapid baseline for initial stiffness but inherently fails to capture parasitic motions or workspace limits. To address these limitations, Pseudo-Rigid-Body Models (PRBMs) approximate flexible segments as rigid links connected by lumped torsional springs [4,5]. While PRBMs are highly effective for conceptual synthesis and large-deflection workspace estimation, they often lack the localized precision required for high-precision flexures and may neglect subtle constraint variations. More advanced variants, such as the 3R model [6] and models specifically handling combined end loads, have been developed to improve approximation accuracy for large-deflection beams. Beam Constraint Models (BCMs) utilize polynomial expansions to capture load-dependent constraints and elastokinematic shortening effects in the intermediate deflection range [7,8]. Recent work on nonlinear complementary strain energy formulations continues to push the accuracy of these models toward larger deflection regimes [9]. For extreme deflections or complex geometries, chained BCM approaches (CBCM) [10,11] and elliptic integral solutions [12] provide higher fidelity, though often at increased computational cost. Building upon these approaches, a general and efficient multiple segment method for the kinetostatic analysis of planar compliant mechanisms has also been proposed [13].

A major challenge remains the systematic selection and validation of these models across a mechanism's full workspace. This is often complicated by the sensitivity of numerical solvers to initial guesses and the inherent trade-offs between speed and accuracy [14]. This paper addresses these challenges by presenting a hierarchical, eight-level multi-fidelity modeling stack. While we utilize the parallelogram flexure mechanism as our primary case study, the underlying technical routine is general and applicable to a wide

[1]Corresponding Author.
March 18, 2026

range of compliant topologies. We implement and cross-validate each level—extending from first-order linear solvers to optimized PRBMs, exact nonlinear Boundary Value Problem (BVP) solvers, and 3D solid FEA. By quantifying the trade-offs in computational speed and predictive accuracy, we provide a validated roadmap that allows designers to navigate the full complexity of static and kinematic mechanism design within a unified framework.

2 Beam Equations

In this section, we derive the exact nonlinear governing equations for a single cantilever beam and a fixed-guided beam.

2.1 Fixed-Free Beam Equations. Consider a flexible cantilever beam of length L, modulus E, and inertia I. We parameterize the beam by its arc length $s \in [0, L]$. The angle between the beam tangent and the x-axis is $\theta(s)$.

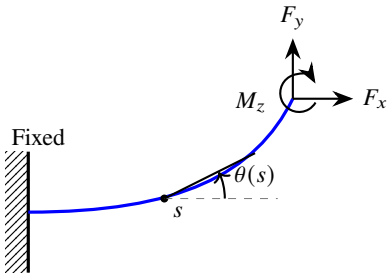

Fig. 1 Cantilever beam under tip loading illustrating kinematic variables

The kinematic relations for an inextensible beam are given by the projection of the tangent onto the coordinate axes:

$$\frac{dx}{ds} = \cos\theta, \quad \frac{dy}{ds} = \sin\theta, \quad \kappa(s) = \frac{d\theta}{ds} \tag{1}$$

Moment equilibrium and the Euler-Bernoulli constitutive law ($M = EI\kappa$) yield the governing second-order ODE:

$$EI\frac{d^2\theta}{ds^2} = F_x \sin\theta - F_y \cos\theta \tag{2}$$

The dimensional governing equations can be generalized by introducing the dimensionless variables defined in Table 1. Substituting these into Eq. (1) and Eq. (2) yields the normalized second-order ODE:

$$\frac{d^2\theta}{d\bar{s}^2} = \alpha_x \sin\theta - \alpha_y \cos\theta \tag{3}$$

Table 1 Normalized Variables for Euler Beam

Variable	Definition	Description
$\bar{s}$	s/L	Norm. arc length $\in [0, 1]$
$\bar{x}, \bar{y}$	$x/L, y/L$	Norm. positions
$\bar{\kappa}$	$L\kappa$	Norm. curvature
α_x, α_y	$F_x L^2/EI, F_y L^2/EI$	Norm. forces
β	$M_z L/EI$	Norm. tip moment

The resulting system consists of Eq. (3) and the normalized kinematic relations $d\bar{x}/d\bar{s} = \cos\theta$ and $d\bar{y}/d\bar{s} = \sin\theta$. This constitutes a boundary value problem (BVP) with boundary conditions at the fixed end ($\bar{x}(0) = 0, \bar{y}(0) = 0, \theta(0) = 0$) and the tip condition ($\theta'(1) = \beta$). This BVP is solved numerically using an iterative BVP solver, such as the shooting method or a collocation-based solver like *solve_bvp*, to obtain the full beam profile and tip displacement for any given loading $(\alpha_x, \alpha_y, \beta)$. While these numerical solvers are remarkably efficient and provide exact results in terms of beam theory, they are sensitive to the initial guess and can struggle to converge under large buckling forces where more than one equilibrium solution may exist (e.g., higher-order buckling modes). Furthermore, while the BVP approach is fast for individual beams, it is often difficult to couple these equations directly with discrete kinematic constraints, such as pin joints, which are common in hybrid compliant-rigid mechanisms. The Python implementation of this solver is publicly available in our GitHub repository.

2.2 Fixed-Guided Beam Equations. The fixed-guided beam is a variation of the cantilever where the tip is constrained to remain flat ($\theta(1) = 0$). This constraint renders the tip moment β an unknown reaction. In normalized form, the problem constitutes an Euler-Bernoulli BVP:

$$\frac{d\mathbf{q}}{d\bar{s}} = \begin{bmatrix} \cos\theta \\ \sin\theta \\ \bar{\kappa} \\ \alpha_x \sin\theta - \alpha_y \cos\theta \end{bmatrix}, \quad \mathbf{q} = \begin{bmatrix} \bar{x} \\ \bar{y} \\ \theta \\ \bar{\kappa} \end{bmatrix} \tag{4}$$

$$\text{BCs: } \bar{x}(0) = \bar{y}(0) = \theta(0) = 0, \quad \theta(1) = 0 \tag{5}$$

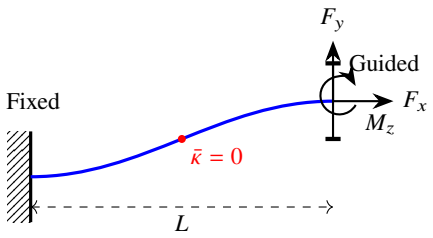

Fig. 2 Fixed-guided beam configuration showing characteristic S-shape deformation and horizontal tip constraint

A fundamental property of this BVP is the *Curvature Antisymmetry Theorem*:

$$\bar{\kappa}(\bar{s}) = -\bar{\kappa}(1 - \bar{s}) \quad \text{for all } \bar{s} \in [0, 1] \tag{6}$$

implying an inflection point at the span midpoint ($\bar{\kappa}(0.5) = 0$). While the curvature $\bar{\kappa}(\bar{s})$ is antisymmetric, the angle $\theta(\bar{s})$ is symmetric about the midpoint ($\theta(\bar{s}) = \theta(1-\bar{s})$), reaching its maximum at $\bar{s} = 0.5$.

This BVP is solved numerically using a collocation method (e.g., *solve_bvp* in Python or *bvp4c* in MATLAB). To ensure robust convergence, the solver is initialized with a cubic displacement guess consistent with the linear Bernoulli-Euler profile for a guided beam:

$$\bar{y}_{init}(\bar{s}) = (3\bar{s}^2 - 2\bar{s}^3)\delta_{linear} \tag{7}$$

where $\delta_{linear} = \alpha_y/12$. The reaction moment is subsequently extracted as $\beta = \bar{\kappa}(1)$. The BVP solver for fixed-free and fixed-guided beams has been implemented in a Python script, which is publicly available in our GitHub repository.

3 Parallelogram Flexure Mechanism

The parallelogram flexure mechanism (Fig. 3) consists of two identical flexible beams, each of length L, modulus E, and inertia I, connected by a rigid platform of width $2W$. Beam 1 and Beam 2 are clamped at global coordinates $(0, W)$ and $(0, -W)$, respectively. In the following sections, we characterize the mechanism behavior using dimensionless parameters that are independent of

absolute geometric and material properties. This enables a universal analysis of normalized deflections $(\bar{s}, \bar{y}, \phi)$ as functions of normalized external loads $(\alpha_x, \alpha_y, \beta)$, providing a performance framework applicable across all flexure scales.

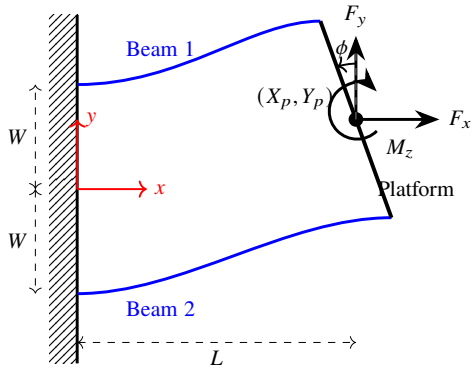

Fig. 3 Parallelogram flexure mechanism under external loading

3.1 Kinematic Constraint and Force Equilibrium Equations. An external load (F_x, F_y, M_z) is applied at the platform center (X_p, Y_p). The static equilibrium of the platform, illustrated in Fig. 4, requires that the horizontal, vertical, and moment reactions from both beams balance the applied external loads. These dimensional relations are subsequently mapped to a dimensionless form to facilitate numerical implementation.

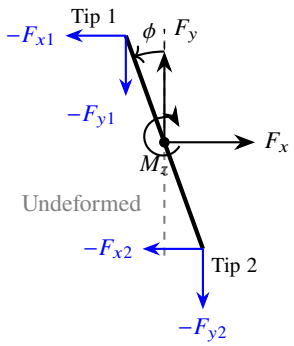

Fig. 4 Free body diagram of the platform ($\phi > 0$)

Table 2 Normalized parameters for the parallelogram mechanism

Parameter	Definition	Description
t	T/L	Norm. beam thickness
w	W/L	Norm. half beam separation
α_{xi}	$F_{xi}L^2/EI$	Norm. horizontal reaction on beam i
α_{yi}	$F_{yi}L^2/EI$	Norm. vertical reaction on beam i
β_i	$M_{zi}L/EI$	Norm. moment on beam i
α_x	F_xL^2/EI	Norm. external horizontal force
α_y	F_yL^2/EI	Norm. external vertical force
β	M_zL/EI	Norm. external moment
u_x	U_x/L	Norm. horizontal displacement
u_y	U_y/L	Norm. vertical displacement
ϕ	–	platform rotation

These static conditions are generalized using the normalized parameters defined in Table 2. The motion of the platform, characterized by a rotation ϕ, imposes displacement and angle compatibility constraints at each beam tip. Together with the force and moment equilibrium, these relations constitute the full system of governing equations summarized in Table 3. The state is found by solving the coupled constraint equations (Table 3) iteratively using a Newton-Raphson scheme where each residual evaluation requires solving two beam BVPs.

The complete system involves six unknowns $(\alpha_{x1}, \alpha_{y1}, \beta_1, \alpha_{x2}, \alpha_{y2}, \beta_2)$ and the platform rotation ϕ, subject to the constraint equations summarized in Table 3.

3.2 Hierarchical Modeling Stack. To solve this problem, we develop a multi-fidelity modeling stack ranging from simple analytical models to high-fidelity FEA simulations. These modeling levels are summarized in Table 4.

In the following, we provide a narrative summary for each modeling level, detailing their formulation, underlying assumptions, and primary role within the design hierarchy:

(1) Linear Beam. This baseline model assumes small-angle approximations ($\sin\theta \approx \theta$) and neglects the fundamental coupling between axial loading and transverse stiffness. It serves as a qualitative reference for infinitesimal deflections.

(2) Beam Constraint Model (BCM). An algebraic model that approximates the exact transcendental beam functions using polynomial expansions. It rigorously captures load-stiffening and elastokinematic shortening, making it ideal for rapid optimization in the intermediate deflection regime.

(3) Guided BVP. A high-fidelity numerical surrogate that solves the exact nonlinear ODEs for a single beam under guided tip constraints. It provides precision for large deflections while assuming synchronized beam motion.

(4) Euler BVP. Our most rigorous analytical solver, treating both beams as coupled nonlinear BVPs. This model captures the differential shortening and axial force asymmetry that drives the platform's parasitic rotation ϕ.

(5) Standard PRBM. A pseudo-rigid-body approximation that replaces flexible segments with rigid links and torsional springs. It facilitates extremely fast mechanism-level synthesis using standard 4-bar linkage kinematics.

(6) Optimized PRBM. A refined PRB model with link parameters optimized against the Euler-Bernoulli ground truth. This level specifically addresses the accuracy degradation of standard PRBM under compressive or near-buckling axial loads.

(7) 2D Beam FEA. A discretized numerical solution using quadratic beam elements. This serves as a primary verification step for the Euler-Bernoulli assumptions in local coordinates without the complexity of shooting-method BVPs.

(8) 3D Solid FEA. The ultimate ground truth, utilizing quadratic tetrahedral elements to capture out-of-plane effects, stress-stiffening, and localized compliance at the base and stage interfaces.

We detail each of these eight solvers in the following sections. All the solvers are implemented in Python and are publicly available in the project GitHub repository at https://github.com/haijunsu-osu/parallelogram_model_comparison.

3.3 Linear Beam. The simplest model assumes small-angle approximations ($\cos\theta \approx 1, \sin\theta \approx \theta$) and neglects the axial-transverse coupling. For the parallelogram mechanism consisting of two identical beams, the stiffness is doubled compared to a single guided beam ($12EI/L^3$), resulting in an equivalent stiffness of $24EI/L^3$. The resulting normalized displacements are:

$$u_y = \frac{\alpha_y}{24}, \quad u_x = 0, \quad \phi = 0 \tag{8}$$

The axial shortening u_x and parasitic rotation ϕ are identically zero in this first-order baseline. This model is implemented in `linear_solver.py` using the `solve_parallelogram` function and is valid only for very small deflections ($\alpha_y \ll 1$).

Table 3 Summary of Equations for the Parallelogram Mechanism

Category	Component	Equation
Beam Physics (for $i = 1, 2$)	Governing ODE	$\theta_i'' = \alpha_{xi} \sin\theta_i - \alpha_{yi} \cos\theta_i$
	Kinematics	$\bar{x}_i' = \cos\theta_i, \quad \bar{y}_i' = \sin\theta_i$
	Fixed BCs	$\bar{x}_i(0) = 0, \bar{y}_i(0) = 0, \theta_i(0) = 0$
	Tip Reaction	$\theta_i'(1) = \beta_i$
Platform Kinematics	Rotation	$\theta_1(1) = \phi, \quad \theta_2(1) = \phi$
	x-Compatibility	$\bar{x}_1(1) - \bar{x}_2(1) = -2w \sin\phi$
	y-Compatibility	$\bar{y}_1(1) - \bar{y}_2(1) = 2w(\cos\phi - 1)$
Mechanism Statics	Horiz. Equil.	$\alpha_{x1} + \alpha_{x2} = \alpha_x$
	Vert. Equil.	$\alpha_{y1} + \alpha_{y2} = \alpha_y$
	Moment Equil.	$\beta_1 + \beta_2 - w\cos\phi\Delta\alpha_x - w\sin\phi\Delta\alpha_y = \beta$
$\Delta\alpha_x \equiv \alpha_{x1} - \alpha_{x2}$; $\Delta\alpha_y \equiv \alpha_{y1} - \alpha_{y2}$ (differential beam loads)		

Table 4 The eight-level hierarchical modeling stack for the parallelogram mechanism

Model	Characteristic / Formulation	Section
Linear Beam	Small-angle, no coupling	Sec. 3.3
BCM [7]	Polynomial expansion, load-stiffening	Sec. 3.4
Guided BVP	Single beam surfing, no ϕ	Sec. 3.5
Euler BVP	Full coupled nonlinear ODEs	Sec. 3.6
PRB (Std.)	($\gamma \approx 0.85, K_\theta = 2.676$)	Sec. 3.7
PRB (Opt.)	($\gamma = 0.90, K_\theta = 2.5$)	Sec. 3.7
FEA (2D)	Nonlinear beam elements (CalculiX)	Sec. 3.8
FEA (3D)	Nonlinear solid elements (CalculiX)	Sec. 3.8

3.4 Beam Constraint Model (BCM). The BCM framework [7], utilizes polynomial expansions to approximate the transcendental beam functions. A key simplification in this approach is the assumption that the beam slope dy/dx remains small (typically less than 10‰, or ≈ 0.1). This allows the exact curvature expression $\kappa = \frac{d^2y/dx^2}{[1+(dy/dx)^2]^{3/2}}$ to be simplified to the linear form $\kappa \approx d^2y/dx^2$. Despite this simplification, the model rigorously captures the nonlinear elastokinematic shortening and load-stiffening effects through axial-load dependent coefficients.

For a symmetric parallelogram mechanism, the closed-form response is:

$$u_y = \frac{\alpha_y}{24 + 1.2\alpha_x} \tag{9}$$

$$u_x = \alpha_x \left(\frac{t^2}{24}\right) - 0.6u_y^2 + \frac{u_y^2 \alpha_x}{1400} \tag{10}$$

$$\phi = \frac{0.5}{w^2}\left[\left(\frac{t^2}{12} + \frac{u_y^2}{700}\right)\left(\beta + u_y(12 + 0.1\alpha_x)\right)\right] \tag{11}$$

where $t = T/L$ is the normalized beam thickness (ratio of cross-section depth T to beam length L, as defined in Table 1). For the benchmark geometry in Table 5, $t = 5/250 = 0.02$. This model is implemented in `bcm_parallelogram.py` and provides a highly efficient closed-form alternative for intermediate deflections.

3.5 Solve for a Single Guided Beam (Guided BVP). This model serves as a high-fidelity surrogate that solves the exact nonlinear beam equations presented in Section 2 for a single beam under a guided tip constraint ($\theta(1) = 0$). It assumes that both beams in the mechanism are identical and undergo synchronized deformation, thereby neglecting the platform-level parasitic rotation ($\phi = 0$). In this simplified implementation, each beam carries exactly half of the normalized loads ($\alpha_x/2$ and $\alpha_y/2$), and any externally applied moment β is ignored as it is balanced by the guided constraint reaction. While it does not capture the coupling that leads to stage rotation, it provides a rigorous solution for large deflections using a numerical Boundary Value Problem (BVP) solver. This model is implemented in `guided_beam_solver.py`.

3.6 Solve for Two Coupled Euler Beams (Euler BVP). The most rigorous analytical approach involves solving the full set of coupled nonlinear equations derived in Section 2 and summarized in Table 3. Unlike the single-beam surrogate, this model treats each beam in the parallelogram individually, solving for their respective internal end loads $(\alpha_{x1}, \alpha_{y1}, \beta_1)$ and $(\alpha_{x2}, \alpha_{y2}, \beta_2)$. This differentiation is critical because the mechanism's geometry and the externally applied loads induce different axial forces in each beam—typically placing one beam in tension while the other is in compression.

By capturing this asymmetry and the resulting differential beam shortening, the model successfully predicts the platform's parasitic rotation angle ϕ. The system of equations is solved using the nested iterative procedure summarized in Algorithm 1. This complete multi-beam solution is implemented in `parallelogram_solver.py` and serves as the ultimate analytical benchmark for our study.

Algorithm 1 Euler BVP Iterative Solver for Parallelogram Mechanism

Initialize: Guess 6 internal loads $\mathbf{p} = [\alpha_{x1}, \alpha_{y1}, \beta_1, \alpha_{x2}, \alpha_{y2}, \beta_2]^\top$.
repeat
  Step 1: Inner Beam BVPs
  for each beam $i = 1, 2$ **do**
    Solve nonlinear ODE $\theta_i'' = \alpha_{xi}\sin\theta_i - \alpha_{yi}\cos\theta_i$
    BCs: $\theta_i(0) = 0$, $\theta_i'(1) = \beta_i$ (shooting or collocation).
    Extract tip state $t_i = [\bar{x}_i(1), \bar{y}_i(1), \theta_i(1)]$.
  end for
  Step 2: Platform Kinematics
  Set platform rotation $\phi \leftarrow \text{avg}(\theta_1(1), \theta_2(1))$.
  Step 3: Residual Evaluation
  Compute residual vector $\mathbf{R}(\mathbf{p}) \in \mathbb{R}^6$ using constraints:
    $\mathbf{R}_1 \leftarrow \theta_1(1) - \theta_2(1)$ (Angle compatibility)
    $\mathbf{R}_2 \leftarrow \Delta\bar{x}(1) + 2w\sin\phi$ (x-compatibility)
    $\mathbf{R}_3 \leftarrow \Delta\bar{y}(1) - 2w(\cos\phi - 1)$ (y-compatibility)
    $\mathbf{R}_{4,5} \leftarrow \sum\alpha_{xi} - \alpha_x, \quad \sum\alpha_{yi} - \alpha_y$ (Equilibrium)
    $\mathbf{R}_6 \leftarrow$ Moment equilibrium (Table 3)
  Step 4: Update
  Update $\mathbf{p}$ via Newton-Raphson: $\mathbf{p} \leftarrow \mathbf{p} - \mathbf{J}^{-1}\mathbf{R}$.
until $\|\mathbf{R}\| < \epsilon$
Result: Platform state $[u_x, u_y, \phi]$.

3.7 Pseudo-Rigid-Body Model (PRBM) (Standard and Optimized). The PRBM approximates large-deflection flexures by replacing flexible segments with rigid pseudo-links and torsional springs [4,5]. For the parallelogram flexure, the entire mechanism is modeled as a 4-bar linkage (Fig. 5), where each beam is represented by a rigid link of characteristic length γL and two horizontal segments of length $(1-\gamma)L/2$. This simplifies the S-shaped deformation into a pure rotary motion of the platform. While higher-order models like Su's 3R model [6] provide superior accuracy for single cantilever beams, the 1R model remains the computational baseline for mechanism-level synthesis. The kinematic relations are defined as:

$$u_y = \gamma \sin\Theta, \quad u_x = \gamma(\cos\Theta - 1) \tag{12}$$

where Θ is the pseudo-rigid-body angle. Each pivot is equipped with a torsional spring of stiffness $K = 2\gamma K_\Theta \frac{EI}{L}$. For the symmetric dual-beam mechanism, the static equilibrium yields a nonlinear transcendental equation for Θ:

$$K\Theta = \frac{F_y}{2}\frac{\gamma L}{2}\cos\Theta \tag{13}$$

where the factors of 2 account for the parallel combination of two beams, with each beam effectively acting as a 1R cantilever under half the total load ($\alpha_y/2$).

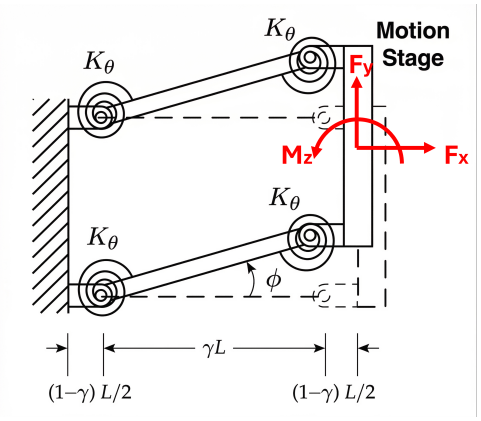

Fig. 5 PRB schematic of the parallelogram flexure. Each beam is modeled as a serial chain of 2R with rigid segments $(1-\gamma)L/2$ and pseudo-links γL. Torsional springs at the pivots have stiffness $K = 2\gamma K_\Theta EI/L$. External loads are applied at the stage center (X_p, Y_p).

The coefficients γ and K_Θ are critical for model accuracy across different loading regimes. While standard textbook values (e.g., $\gamma = 0.8517$ for fixed-guided beam with a vertical end force) work well for moderate deflections, they often fail to capture the behavior under high axial prestress or near-buckling conditions. Consequently, an optimized set of parameters was obtained by minimizing the Root-Mean-Square Error (RMSE) of the transverse deflection u_y relative to the nonlinear Euler BVP ground truth over a sweep of $\alpha_y \in [-15, 15]$ (see `gamma_study.py`). As shown in Table 4, the optimized model utilizes a higher γ factor (0.900), which better approximates the "softening" effect and shape changes caused by internal buckling forces. This optimization improves the prediction of vertical stiffness and kinematic shortening u_x with K_Θ refined to 2.5. The model is implemented in `prb_parallelogram.py` using a numerical solver for Eq. (13).

3.8 Finite Element Analysis (FEA) 2D and 3D. The final two levels of the hierarchy utilize numerical discretization to provide high-fidelity verification and ground-truth validation. Both 2D and 3D FEA models are implemented using the open-source solver `CalculiX` with the geometrically nonlinear (NLGEOM) solver option enabled. Since these numerical solvers operate on absolute dimensions, the benchmark mechanism is modeled using the geometric and material properties summarized in Table 5 (structural steel). The external moment β is applied via a horizontal force couple at $y = \pm 10$ mm for 3D and $y = \pm 50$ mm for 2D relative to the stage center. The setup parameters for both models are summarized in Table 6.

Table 5 Benchmark Model Parameters

Param.	Value	Param.	Value
L	250.0 mm	E_{beam}	210.0 GPa
W	75.0 mm	E_{stage}	5000.0 GPa
H	50.0 mm	ν	0.3
T	5.0 mm	L_m	50.0 mm
I_{beam}	520.83 mm^4		

Table 6 FEA Simulation Setup Parameters

Parameter	2D Model	3D Model
Element Type	B32 (Quadratic Beam)	C3D10 (Quadratic Tet)
Mesh Size	$L_c = 6.5$ mm	10 mm (Global)
Mesh Order	2nd	2nd
Nonlinearity	NLGEOM	NLGEOM
Platform	Quasi-Rigid	Quasi-Rigid

The 2D FEA utilizes quadratic beam elements with a characteristic mesh length of 6.5 mm ($L_c = 6.5$ mm) for both the flexures and the platform stage. The motion stage is modeled as a rigid coupling between the beam tips, accurately representing the $2W$ linkage constraint. This level serves as a verification for the Euler-Bernoulli assumptions in local coordinates without Section 2's shooting method complexity.

The 3D ground truth model uses solid elements to capture stress-stiffening, out-of-plane effects, and the localized compliance of the base/stage interfaces. To ensure numerical stability and accuracy for the large-scale parametric sweep, a mesh convergence study was performed for a nominal load case ($\alpha_x = 0, \alpha_y = 5, \beta = 0$). As shown in Table 7, the displacement and rotation values converge monotonically as the mesh size is refined from 10 mm to 3 mm. Using the 3 mm mesh as a high-fidelity reference, the 10 mm mesh exhibits a relative error of only 0.60% for the primary transverse deflection u_y and 1.72% for the parasitic rotation ϕ. Crucially, the 10 mm mesh solve time is over 45 times faster than the 3 mm mesh, enabling the execution of thousands of load cases in a reasonable timeframe. Thus, the 10 mm global mesh size was selected as the optimal trade-off for generating the ground-truth dataset.

Table 7 Mesh convergence study for 3D FEA

Mesh Size	Elements	Solve Time (s)	Rel. Err. (y)
10 mm	4,878	38.1	0.60%
7.5 mm	10,000	82.3	0.35%
5 mm	24,558	222.5	0.21%
4 mm	45,332	511.6	0.07%
3 mm (Ref.)	95,810	1,739.9	—

The monolithic geometry includes integrated base blocks and the stage, allowing for a complete assessment of the analytical models against full-scale solid mechanics simulations. The implementation scripts for running these FEA solvers are publicly available in our GitHub repository.

4 Data Generation and Runtime Comparison

4.1 Data Generation. A benchmark loading grid was established to verify the reduced-order models. The simulation sweep consists of 1,517 distinct load cases covering the normalized ranges summarized in Table 8. Both 2D beam and 3D solid FEA solvers were executed across this entire grid to generate ground-truth displacement fields.

To ensure complete coverage of the bilateral workspace, the simulation data were augmented using mirror symmetry about the x-axis. While the primary FEA sweep was computed for positive transverse loads ($\alpha_y \geq 0$), the negative range ($\alpha_y < 0$) was derived using the mapping $(\alpha_y, \alpha_x, \beta) \rightarrow (-\alpha_y, \alpha_x, -\beta)$, which corresponds to a response mapping of $(u_x, u_y, \phi) \rightarrow (u_x, -u_y, -\phi)$. This augmentation effectively doubles the dataset to 3,094 load points, covering the full symmetric range $\alpha_y \in [-20, 20]$.

Table 8 Normalized Load and Geometry Sweep Grid Ranges

Para.	Type	Discrete Values
α_y	Load	$\{0, 0.5, 1, 2, \ldots, 10, 12, \ldots, 20\} \cup$ Symmetric
α_x	Load	$\{-10, -5, -4, -3, -2, -1, 0, 1, 2, 3, 4, 5, 10\}$
β	Load	$\{-3, -2, -1, 0, 1, 2, 3\}$
t	Geom.	$T/L = 5/250 = 0.02$ (fixed for benchmark)
w	Geom.	$W/L = 75/250 = 0.30$ (fixed for benchmark)

The 3D FEA data generation utilized parallel execution with 10 worker processes, completing the 1,547-case sweep in approximately 3 hours of wall-clock time (integrated solver time of 19.02 hours). In contrast, the 2D FEA sweep was executed on a single CPU core, requiring approximately 32.5 minutes (0.54 hours) to complete. The complete multi-fidelity dataset, including raw FEA outputs and pre-processed analytical results, is publicly available on the project's GitHub repository for further analysis and benchmarking.

4.2 Computational Efficiency Comparison. The performance of each modeling level is summarized in Table 9, using the 3D solid FEA as the baseline for computational speedup.

Table 9 Computational Performance and Speedup vs. 3D FEA

Model	Succ. Rate	Mean time (s)	Speedup
FEA 3D	1547 / 1547	4.43E+01	1.00
FEA 2D	1547 / 1547	1.26E+00	35.14
Euler BVP	1425 / 1547	2.86E+00	15.46
Guided Beam	1547 / 1547	3.17E-03	1.40E+04
PRB (Std/Opt)	1547 / 1547	~1.00E-04	~4.50E+05
BCM	1547 / 1547	3.45E-06	1.28E+07
Linear	1547 / 1547	3.73E-07	1.18E+08

The efficiency analysis reveals a dramatic spread in computational cost across the stack. While high-fidelity 3D FEA requires tens of seconds per case, the closed-form BCM and Linear models achieve speedups of seven to eight orders of magnitude ($> 10^7\times$). It is important to note that the Euler BVP model failed to converge in 122 cases (a 92% success rate). This highlights the trade-off between the mathematical rigor of the S-shaped BVP solution and the robust numerical stability of FEA or the algebraic stability of BCM.

Euler BVP Failure Domain. The 122 non-convergent cases are not uniformly distributed across the load grid; they cluster in two well-defined regions. First, under high compressive axial loads ($\alpha_x \lesssim -3$) combined with small transverse loads ($\alpha_y < 2$), the parallelogram beams operate near or beyond the first Euler buckling load ($\alpha_{x,cr} = -\pi^2 \approx -9.87$ for a fixed-guided beam), where the BVP Jacobian becomes ill-conditioned and multiple equilibrium branches coexist. Second, at very large transverse deflections ($\alpha_y > 15$) combined with tensile axial loads ($\alpha_x > 5$), the collocation solver's cubic initialization deviates excessively from the true solution, causing the Newton-Raphson outer loop to diverge. In both regions, the 2D and 3D FEA solvers converge robustly due to their incremental load-stepping strategy, underscoring their role as the reliable ground truth for extreme load cases.

4.3 Interactive Visualization and Benchmarking App. To facilitate real-time exploration of the modeling hierarchy, we developed an interactive Python-based application (`compare_models_gui.py`). This tool allows users to manually adjust loading parameters $(\alpha_x, \alpha_y, \beta)$ and geometric dimensions (such as the normalized separation w) using sliders, providing immediate visual feedback on the resulting mechanism deformation. While this app is specifically tailored for parallelogram flexures, other software tools such as DAS-2D [15] have been developed for the concept design and analysis of more general compliant mechanisms.

As shown in Fig. 6, the app overlays the deformed shapes predicted by each model in the hierarchy. This visual comparison is particularly useful for identifying the limits of linearity and the onset of axial shortening (u_x). The interface also includes a live comparison table that reports the primary displacements (u_x, u_y, ϕ) and computes percentage errors relative to the high-fidelity 3D FEA benchmark.

A notable feature is the integration of "live" solvers: while many results are retrieved from pre-computed sweeps for speed, the app can also invoke the FreeCAD-based FEA and Euler BVP solvers on-demand for arbitrary load cases. It is important to note that for the BCM level, the visualized beam shape is nominal (based on standard cubic interpolation) because the model's fundamental output is the platform's pose (u_x, u_y, ϕ) rather than the internal beam discretization.

The development of this interactive tool and the underlying solver stack was significantly accelerated through the assistance of an AI coding agent (based on the OpenAI's Codex 5.4 model), which aided in the construction of the Matplotlib-based GUI Fig. (6,7) and the orchestration of the cross-platform FEA scripts. The complete application, including all multi-fidelity solvers and benchmark datasets, is publicly available on the project's GitHub repository. This tool serves as a powerful benchmarking platform for validating low-fidelity models against rigorous numerical solutions across the entire workspace.

4.4 FEA 3D Axial Load Sweep Analysis. To further characterize the multi-fidelity performance, we conducted an extensive axial load sweep using the 3D FEA ground-truth model. The compressive load α_x was varied from -10 (near buckling) to 10 (tensile), with the transverse load α_y sweeping from 0 to 20. As shown in Fig. 8, the axial load exerts a profound influence on the system compliance and geometric coupling.

The transverse response u_y vs. α_y (Fig. 8a) highlights the *softening* and *stiffening* effects of axial loads. Negative α_x (compression) significantly increases the transverse compliance, with the $\alpha_x = -10$ case yielding a 30.3% larger deflection at $\alpha_y = 20$ compared to the pure transverse loading case ($\alpha_x = 0$). Conversely, positive α_x (tension) stiffens the mechanism, reducing the deflection by 20.4% at the maximum load. This spread confirms that the linear beam baseline, which remains invariant to α_x, serves only as a qualitative reference and fails to capture the essential load-stiffening physics.

The parasitic rotation ϕ (Fig. 8c) is the most sensitive metric to axial loading. At $\alpha_y = 20$, the rotation for the compressive case $\alpha_x = -10$ is approximately 4.34× larger than the $\alpha_x = 0$ value and 11.4× larger than the tensile case $\alpha_x = 10$. This explosive growth in parasitic rotation as the system approaches its critical load underscores the necessity of high-fidelity 3D modeling for precision

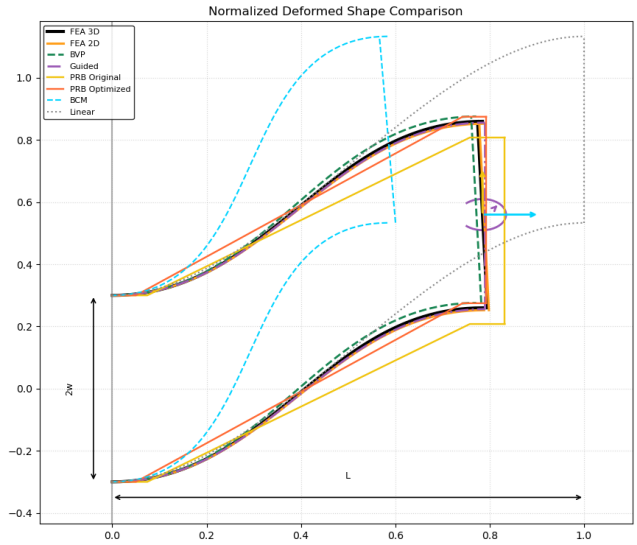

Fig. 6 Screenshot of the interactive benchmarking app showing the normalized deformed shapes for multiple models. The plots shows the deformed shapes for $\alpha_x = 0, \alpha_y = 20, \beta = 0$. The maximum lateral deflection is about $u_y = 0.55$ or 55% of the beam length.

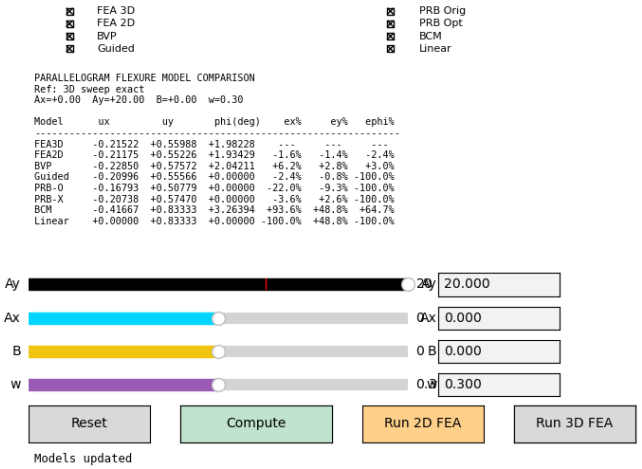

Fig. 7 User interface of the interactive benchmarking app. The control panel (bottom) includes sliders for loading and geometry, model visibility toggles, and buttons for live FEA triggering.

engineering, where even milliradian-scale errors can result in performance failure.

5 Accuracy Assessment and Comparative Studies

We conduct a comprehensive comparative study to evaluate the accuracy and efficiency of the eight-level modeling stack.

5.1 Case 1: $\alpha_x = \beta = 0$. The first case considers pure transverse loading (α_y) in the absence of axial forces and external moments. This scenario isolates the primary stiffness and kinematic shortening effects.

The primary stiffness response (u_y vs. α_y) as shown in Fig. 9a is captured accurately by most models in the small deflection regime ($|\alpha_y| < 5$), with the BCM and Euler BVP models providing MAPEs of 4.8% and 3.8% respectively. However, as the loading increases ($5 \leq |\alpha_y| \leq 20$), the accuracy of the algebraic BCM model degrades; its range-based MAPE reaches 23.3%. Specifically, the standard PRB model for y-deflection exhibits an error of 15.3% in the small deflection regime, which notably reduces to 12.1% in the large deflection range, indicating that the model is effectively optimized for overall performance across a very large range of motion. The optimized PRB model consistently outperforms both the standard PRB (1.0% MAPE for $|\alpha_y| < 5$) and BCM across the force range. In contrast, the Euler BVP model and 2D FEA maintain high accuracy throughout the workspace, with MAPEs below 3.4% and 1.1% respectively even at extreme deflections.

The kinematic shortening effect (u_x vs. α_y, Fig. 9b) reveals a clear divergence in model fidelity. By definition, the Linear model fails to capture any axial shortening, resulting in a consistent 100% relative error. In contrast, both the Euler BVP and 2D FEA models capture the parabolic shortening trend with high precision, maintaining MAPEs within 7.0% and 1.6% respectively across both ranges. While the PRB models and the Guided Beam approximation perform well (with optimized PRB error reducing to 4.0% for $5 \leq |\alpha_y| \leq 20$), the algebraic BCM model exhibits significant performance degradation at higher loads. The BCM's range-based MAPE for u_x starts at 8.8% in the small-deflection regime but grows to 43.0% as the loading approaches the workspace limits, underscoring its limitations in capturing second-order kinematic couplings at extreme deflections.

A critical result is observed in the prediction of parasitic rotation ϕ (Fig. 9c). While the 3D FEA reveals a small but non-zero rotation reaching approximately 0.4°, the low-order models (Guided Beam, Linear, and PRB) assume zero rotation by definition, leading to 100% relative error in this metric. The Euler BVP model, which accounts for the differential shortening between the two beams, predicts ϕ with increasing accuracy as the deflection grows, with its MAPE dropping from 74.9% for $|\alpha_y| < 5$ to 11.4% in the large-deflection regime. 2D FEA remains the most accurate non-reference model for ϕ, with MAPEs consistently between 2% and 4%.

A comparison between the PRBM and BCM models highlights their relative advantages for parallelogram flexure modeling. The BCM is generally more accurate in the small-to-moderate loading range ($\alpha_y \in [0, 5]$); however, for larger deformations, the standard PRB model provides better scaling for the primary stiffness. Notably, the optimized PRB model outperforms the BCM in predicting both u_y and u_x across the entire loading range. The relative error percentages for these models are summarized in Fig. 10. It must be emphasized, however, that all PRB-based models are inherently limited by their simplified kinematics and cannot predict the parasitic rotation ϕ.

5.2 Case 2: $\alpha_x = -5, \beta = 0$. In Case 2, we introduce a more severe compressive axial load ($\alpha_x = -5$), which further challenges the analytical models as the system approaches the buckling limit. The primary transverse displacement u_y (Fig. 11a) demonstrates significant divergence in algebraic model fidelity. The BCM exhibits massive error growth, reaching a range-based MAPE of 36.9% at higher deflections ($5 \leq |\alpha_y| \leq 20$) as the quadratic load-stiffening approximations fail to capture the severe axial-transverse coupling. Interestingly, the Linear model (20.0% in R1, 13.1% in R2) and the optimized PRB model (22.9% in R1, 15.2% in R2) provide more robust albeit less precise estimates than the BVP-based solvers. The Euler BVP model maintains high accuracy (MAPE ~4.5%) but suffers from numerical instability, failing to converge at the maximum load of $\alpha_y = 20$.

The kinematic shortening u_x (Fig. 11b) is extremely sensitive to this higher compressive load. The algebraic BCM fails dramatically in this regime, with its MAPE for shortening reaching 72.0% in the large-deflection range. This confirms that polynomial expansions for elastokinematic shortening are insufficient when axial compression is high. In contrast, the Guided Beam and Euler BVP models remain more reliable, with range-based MAPEs within 8.5% and 7.6% respectively. The optimized PRB model also

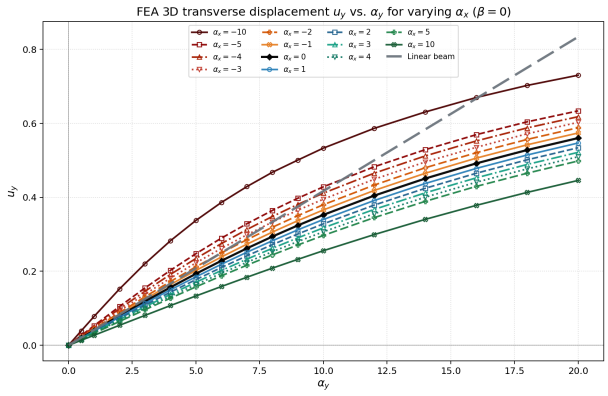

(a)

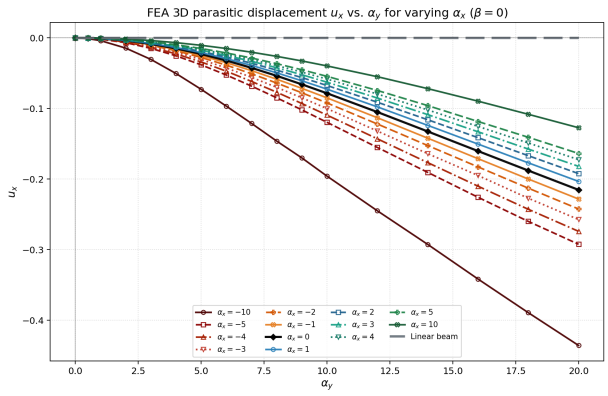

(b)

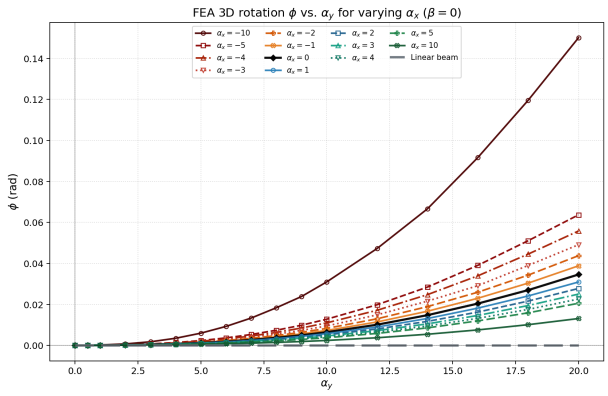

(c)

Fig. 8 FEA 3D parametric sweep of axial load $\alpha_x \in [-10, 10]$ showing the softening (compressive) and stiffening (tensile) effects on the mechanism response, u_y, u_x, ϕ vs. $\alpha_y \in [0, 20]$.

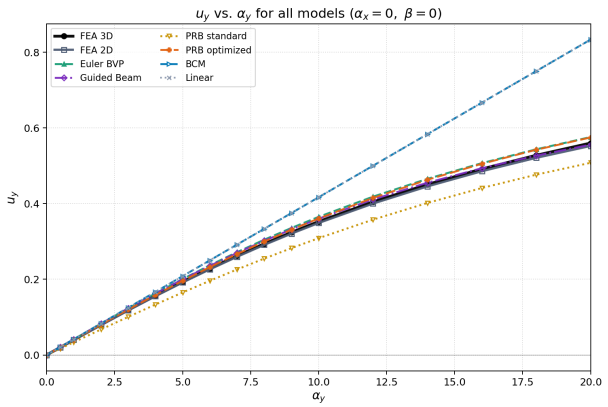

(a)

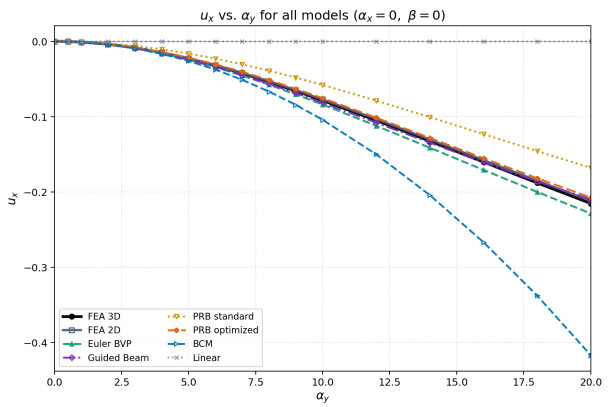

(b)

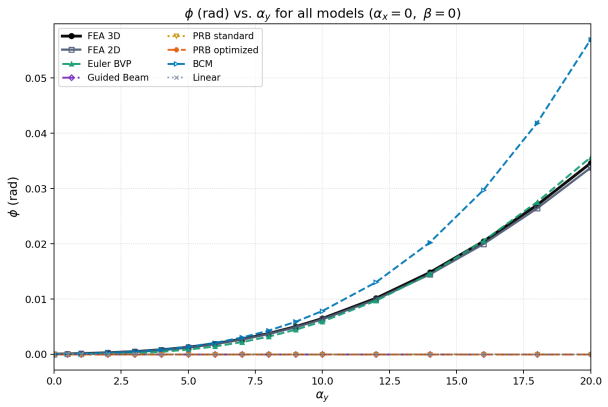

(c)

Fig. 9 Mechanism response u_y, u_x, ϕ vs. $\alpha_y \in [0, 20]$ under pure transverse loading ($\alpha_x = \beta = 0$). The low-order models fail to capture the parasitic rotation ϕ.

shows reasonable performance with a MAPE of 36.2% for large deflections, significantly outperforming the Linear model which predicts zero shortening.

The parasitic rotation ϕ (Fig. 11c) highlights the absolute necessity of high-order models for precision applications. While most models (Linear, PRB, Guided Beam) predict zero rotation by definition, the 3D FEA ground truth shows rotation values that are significantly amplified by the axial compression. The BCM provides a rough estimate of the rotation trend but with its MAPE jumping from 2.4% for $|\alpha_y| < 5$ to 42.3% at larger deflections. The detailed error distributions across the loading range are shown in Fig. 12. These failures near the buckling threshold underscore that while algebraic models are excellent for conceptual synthesis, high-fidelity BVP or FEA validation is mandatory for mechanisms operating under significant compressive stress.

5.3 Case 3: $\alpha_x = 0, \beta = 3$. In Case 3, we examine the system's accuracy under a pure external moment ($\beta = 3$) in the absence of axial loads. This scenario highlights the models' ability to capture purely rotational and cross-coupled effects. As with Case 2, certain high-fidelity models like the Euler BVP exhibit convergence challenges under these specific loading conditions, failing at $\alpha_y = 18$ and 20.

The relative error in u_y (Fig. 13a) shows that the optimized PRB model provides exceptional performance, with range-based

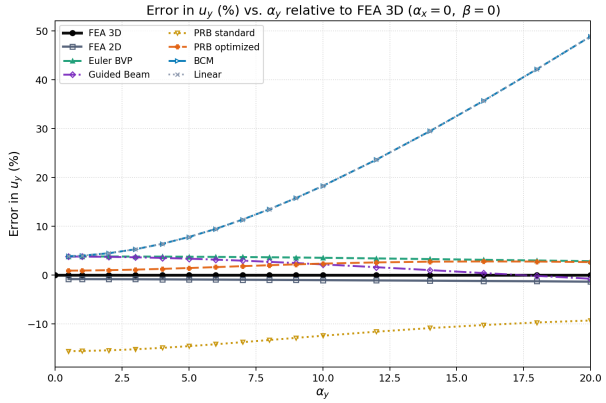

(a)

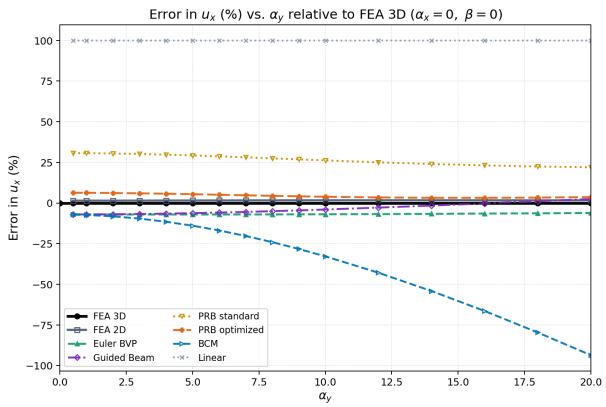

(b)

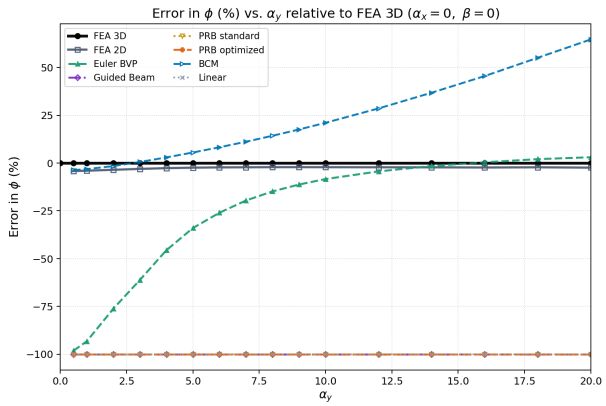

(c)

Fig. 10 Relative error percentages of u_y, u_x, ϕ vs. $\alpha_y \in [0, 20]$ for modeling levels under pure transverse loading ($\alpha_x = \beta = 0$) relative to the 3D FEA ground truth.

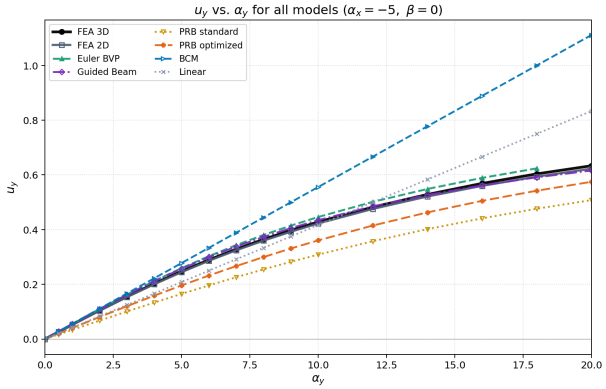

(a)

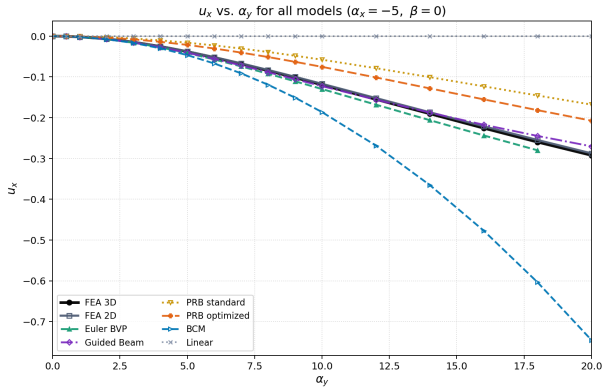

(b)

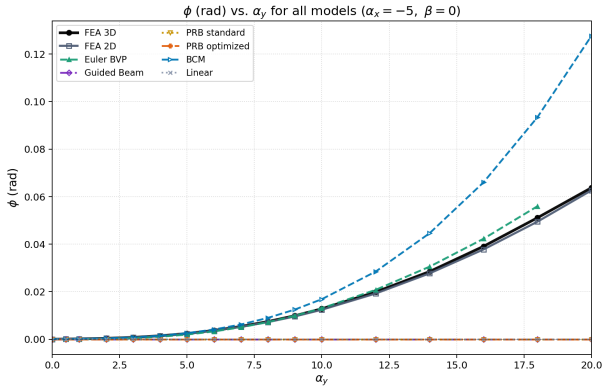

(c)

Fig. 11 Mechanism response u_y, u_x, ϕ vs. $\alpha_y \in [0, 20]$ under compressive axial loading ($\alpha_x = -5, \beta = 0$). The models exhibit significant divergence as the system approaches the buckling limit.

MAPEs as low as 0.3–0.5%. This indicates that the optimized γ factor is highly effective even when external moments are present. In contrast, the BCM and Linear models both exhibit range-based MAPEs between 3.6% and 21.1%, demonstrating a lack of sensitivity to the moment-driven softening or stiffening that the high-order models capture.

For kinematic shortening u_x (Fig. 13b), the Guided Beam and updated Euler BVP models remain the most accurate analytical predictors, with range-based MAPEs between 3.3% and 7.0%. The optimized PRB model also maintains a reasonable error (7.9–8.2%), while the Linear model remains completely invalid (100% error).

The parasitic rotation ϕ (Fig. 13c) under external moments reveals a "sweet spot" for the BCM model. Despite the simplified kinematics of algebraic approaches, the BCM achieves a MAPE of 0.8% for small deflections, growing to 17.3% for larger deflections. This is significantly better than its performance under compressive loads. Most other low-order models (Linear, PRB, Guided Beam) predict the same rotation value by definition, leading to a 100% relative error as they fail to capture the additional rotation induced by the flexure's differential shortening.

The complete comparative reports for these and additional load cases, including detailed error tables and convergence data, are publicly available in our GitHub repository [16] to support further

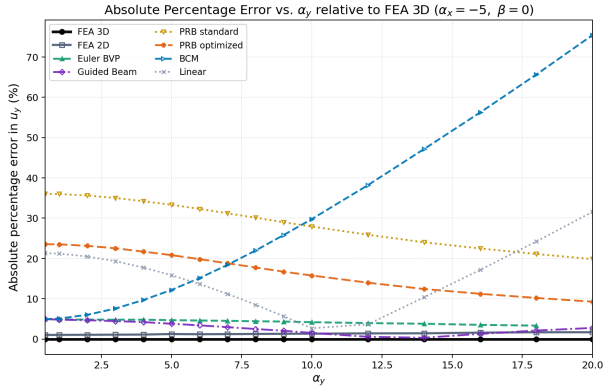

(a)

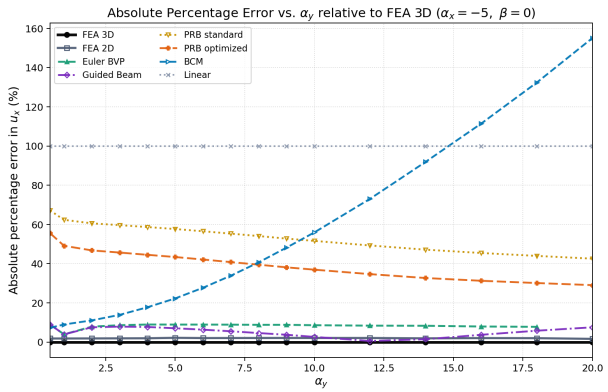

(b)

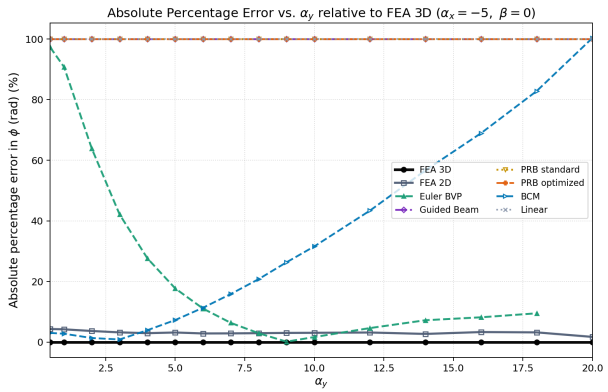

(c)

Fig. 12 Relative error percentages of u_y, u_x, ϕ vs. $\alpha_y \in [0, 20]$ for modeling levels under compressive axial loading ($\alpha_x = -5, \beta = 0$) relative to the 3D FEA ground truth.

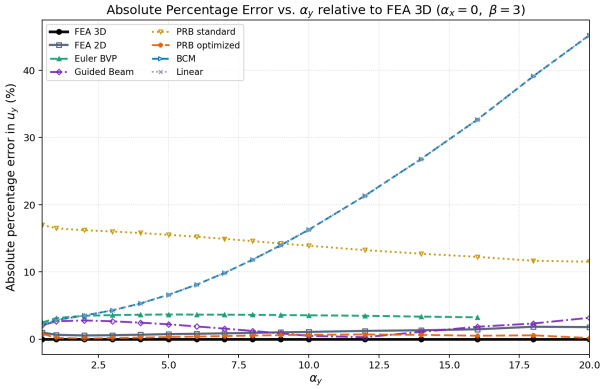

(a)

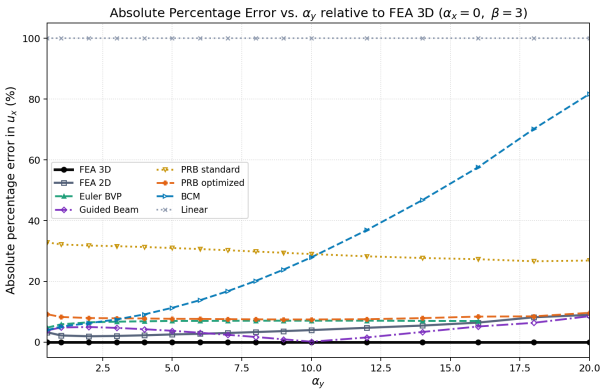

(b)

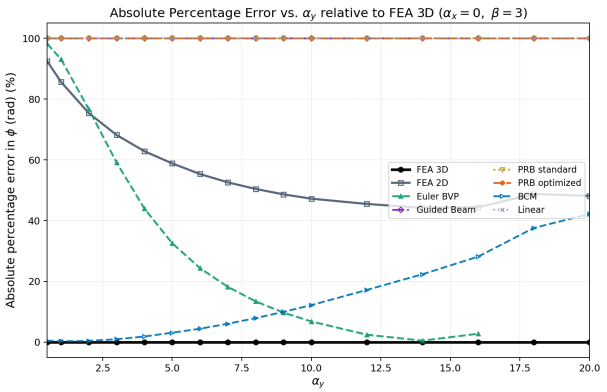

(c)

Fig. 13 Relative error percentages of u_y, u_x, ϕ vs. $\alpha_y \in [0, 20]$ for modeling levels under external moment loading ($\alpha_x = 0, \beta = 3$) relative to the 3D FEA ground truth.

multi-fidelity research.

6 Discussions

In this section, we consolidate the error metrics across different modeling fidelities and provide practical recommendations for model selection based on computational and accuracy requirements.

6.1 Summary of Model Errors. Table 10 provides a consolidated summary of the mean absolute percentage error (MAPE) for the horizontal displacement u_x, transverse displacement u_y, and parasitic rotation ϕ. The errors are reported for three representative cases: Case 1 (pure transverse loading), Case 2 (compressive axial loading $\alpha_x = -5$), and Case 3 (external moment loading $\beta = 3$). To highlight the performance limits of the models, each case is broken down into a small-deflection range ($|\alpha_y| < 5$) and a large-deflection range ($5 \leq |\alpha_y| \leq 20$).

The granular accuracy analysis in Table 10 reveals distinct regimes of model superiority based on the presence of axial loading. In the absence of axial forces (Cases 1 and 3), the **Optimized PRB model (L6)** consistently outperforms the BCM (L2) for the primary transverse displacement u_y. For instance, in Case 3, the optimized PRB achieves a near-perfect MAPE of 0.3–0.5%, whereas the BCM exhibits errors between 3.6% (small deflection) and 21.1% (large deflection). Furthermore, for kinematic shortening u_x, the optimized PRB (4.0% in Case 1, R2) remains more

Table 10 Consolidated Error Summary (MAPE in %) relative to 3D FEA ground truth. Each cell reports accuracy metrics in the format (u_y / u_x / ϕ).

Model Level	Case 1 ($\alpha_x = 0, \beta = 0$)		Case 2 ($\alpha_x = -5, \beta = 0$)		Case 3 ($\alpha_x = 0, \beta = 3$)	
	$\lvert\alpha_y\rvert < 5$	$5 \le \lvert\alpha_y\rvert \le 20$	$\lvert\alpha_y\rvert < 5$	$5 \le \lvert\alpha_y\rvert \le 20$	$\lvert\alpha_y\rvert < 5$	$5 \le \lvert\alpha_y\rvert \le 20$
L1: Linear Beam	4.8 / 100 / 100	23.3 / 100 / 100	20.0 / 100 / 100	13.1 / 100 / 100	3.6 / 100 / 100	21.1 / 100 / 100
L2: BCM	4.8 / 8.8 / 2.4	23.3 / 43.0 / 28.0	6.7 / 11.8 / 2.4	36.9 / 72.0 / 42.3	3.6 / 6.4 / 0.8	21.1 / 36.9 / 17.3
L3: Guided Beam	3.7 / 6.9 / 100	1.9 / 3.6 / 100	4.6 / 7.2 / 100	2.1 / 4.4 / 100	2.5 / 4.5 / 100	1.5 / 3.3 / 100
L4: Euler BVP[†]	3.8 / 7.0 / 74.9	3.4 / 6.8 / 11.4	4.9 / 7.6 / 64.3	4.1 / 8.5 / 6.9	3.2 / 6.1 / 74.2	3.5 / 7.0 / 12.3
L5: PRB (Std.)	15.3 / 30.3 / 100	12.1 / 25.7 / 100	35.4 / 61.6 / 100	27.0 / 50.6 / 100	16.3 / 31.9 / 100	13.6 / 28.8 / 100
L6: PRB (Opt.)	1.0 / 6.1 / 100	2.3 / 4.0 / 100	22.9 / 48.3 / 100	15.2 / 36.2 / 100	0.3 / 8.2 / 100	0.5 / 7.9 / 100
L7: FEA 2D	0.9 / 1.4 / 3.5	1.1 / 1.6 / 2.3	1.1 / 1.9 / 3.7	1.4 / 2.0 / 2.9	0.7 / 2.3 / 76.8	1.2 / 4.8 / 49.4
L8: FEA 3D (Ref.)	— / — / —	— / — / —	— / — / —	— / — / —	— / — / —	— / — / —

[†] MAPE calculated only for convergent cases; L4 fails to converge in extreme compression/deflection regimes.

robust than the BCM (43.0% in Case 1, R2) at extreme deflections, confirming that the γ-factor optimization effectively compensates for the lack of higher-order kinematic terms in PRB models.

Furthermore, the table highlights a significant advantage of the **BCM (L2)** in predicting the parasitic rotation ϕ at small deflections. Across all three cases for $|\alpha_y| < 5$, the BCM achieves the lowest rotation error (ranging from 0.8% to 2.4%), even outperforming the high-fidelity numerical solvers like 2D FEA in this specific regime. This is because the BCM's algebraic formulation directly accounts for the primary cross-axis stage rotation, whereas numerical solvers and zero-rotation models (PRB, Guided Beam) either suffer from sensitivity at small scales or ignore the effect entirely.

However, the relative performance shifts significantly when compressive axial loads are introduced (Case 2). In the small deflection regime ($|\alpha_y| < 5$), the **BCM (L2)** remains superior for all metrics, maintaining a MAPE of 6.7% for u_y and 11.8% for u_x alongside its market-leading rotation prediction. By comparison, the optimized PRB (L6) suffers from 22.9% and 48.3% errors respectively for the primary displacements. This confirms that the BCM's load-stiffening parameters are well-suited for capturing the initial stages of buckling-induced compliance. Conversely, as the system enters the large deflection regime ($5 \le |\alpha_y| \le 20$) under compression, the BCM's accuracy collapses, with shortening and rotation errors growing sharply (e.g., reaching 42.3% for ϕ). In this extreme regime, the **Optimized PRB (L6)** becomes the more reliable tool for primary displacements, while high-order BVP or FEA solvers become mandatory for accurate rotation sensing. This crossover behavior underscores that while BCM is excellent for initial-buckling synthesis and small-deflection rotation sensing, the Optimized PRB is the preferred rapid-solver for exploring the mechanism's bilateral limits under stress.

6.2 Model Selection Guide. The quantitative assessment across the modeling stack enables the definition of a validated roadmap for designers. Based on the performance spread and error localization, we provide the following recommendations:

(1) **Rapid Synthesis and Optimization:** For computationally demanding tasks such as design synthesis, optimization, or real-time control where computational budgets are restricted, the **Beam Constraint Model (BCM)** is recommended for small to intermediate deflections ($|\alpha_y| < 5$), particularly when predictions of shortening u_x and stage rotation ϕ (under non-compressive loads) are required.
(2) **Large Deflection Analysis:** When operating in the large deflection regime ($5 \le |\alpha_y| \le 20$), the **Optimized PRB model** provides the best balance of speed and robustness. It operates in sub-millisecond runtimes while maintaining errors typically below 5% for transverse displacement in non-compressive cases, making it suitable for both analysis and synthesis in expansive workspaces.
(3) **High-Fidelity Screening:** For final design validation or high-precision analysis where a local mesh-based solver is available (e.g., FreeCAD/CalculiX), **2D Beam FEA** is recommended. It provides excellent accuracy (1–5%) throughout the deflection range even up to $\alpha_y = 20$ with rapid solve times (1–2 seconds). If FEA solver is not available, **Euler BVP beam solver** is recommended.
(4) **Interactive Design and Parasitic Analysis:** For interactive design tools requiring high-fidelity feedback on the parasitic rotation ϕ, the **Guided Beam solver** (~3 ms) or the **Euler BVP solver** should be utilized. If stage rotation prediction is not strictly required, the **Optimized PRB** is more numerically robust than the Euler BVP near buckling limits and should be preferred for workspace exploration.

7 Data Availability

All the datasets, modeling scripts, interactive analysis app, benchmark reports and comparative studies are available at the project repository [16].

8 Conclusions

We presented an open-source, hierarchical, eight-level multi-fidelity modeling stack for the design and analysis of compliant parallelogram mechanisms. By systematically organizing model fidelities from first-order linear beam to high-fidelity 3D solid FEA, we provide a unified framework that bridges the gap between rapid conceptual synthesis and rigorous physical validation. To empower the community, the entire solver stack, benchmark data, and interactive visualization tools are released as an open-source project. This structured pathway allows the Beam Constraint Model and optimized PRBM to serve as the "sweet spot" for conceptual design—providing kinematic nonlinearities with relatively less computational complexity indispensable for iterative synthesis.

Our study confirms that while low-order models capture primary stiffness, they often fail to predict second-order geometric couplings, such as the parasitic rotation ϕ. Thus, the eight-level stack ensures that rapid design iterations are systematically validated using the upper numerical and FEA levels.

While the parallelogram flexure served as the specific benchmark, the systematic cross-validation of modeling levels constitutes a general technical routine applicable to broader classes of compliant mechanisms. Based on the summary of the benchmark test results, a comprehensive model selection guide is concluded to assist designers in choosing the most appropriate fidelity level based on their specific accuracy and computational constraints. The core contributions and findings of this work are summarized as follows:

(1) **Validated Hierarchy:** We successfully implemented and cross-validated eight disparate modeling levels, including algebraic (Linear Beam, BCM, PRBM), transcendental (Guided Beam), and numerical (Euler BVP, FEA) approaches. Each level captures progressively more complex phenomenon, from simple stiffness to parasitic rotations and shortening.
(2) **Performance Tradeoffs:** Our runtime analysis demonstrated a performance spread of over eight orders of magnitude.

While 3D FEA requires ∼44 seconds per load case, the algebraic BCM and Linear Beam models achieve near-instantaneous evaluation ($< 10^{-6}$ s), enabling massive-scale design optimization.

(3) **Optimized PRBM:** We demonstrated that standard PRB parameters often underpredict deflections under high loads for parallel guided mechanisms. By utilizing an optimized factor ($\gamma = 0.90$) derived from a systematic parametric sweep, we significantly improved the model's accuracy under axial compressive loads without increasing computational complexity.

(4) **Buckling & Nonlinear Effects:** Comparative studies (Cases 1 & 2) highlighted the critical impact of axial loading. While BCM is highly efficient for moderate deflections ($|\alpha_y| < 5$), its accuracy degrades rapidly near the buckling threshold. Under high axial compression, even the optimized PRB exhibits significant errors in predicting u_x and u_y across both small and large deflection ranges ($|\alpha_y| \in [0, 20]$), underscoring the limitations of standard algebraic models in the buckling regime.

(5) **Interactive Open Source Benchmarking:** The development of an open-source interactive app and a public dataset of over 3,000 load cases [16] provides the community with a robust, transparent baseline for future multi-fidelity research.

Future work will focus on integrating these disparate modeling levels into a single, adaptive framework that automatically switches between fidelities based on real-time assessments of required computational efficiency, predictive accuracy, and deformation scale. Furthermore, the generated dataset of over 3,000 load cases provides a robust foundation for training specialized machine learning models dedicated to the rapid design synthesis of compliant parallelogram mechanisms. Such models could facilitate instantaneous synthesis while satisfying stringent industry requirements for both efficiency and accuracy across large workspaces.

References

[1] Howell, L. L., 2001, *Compliant Mechanisms*, John Wiley & Sons.

[2] Howell, L. L., Magleby, S. P., and Olsen, B. M., 2013, *Handbook of Compliant Mechanisms*, John Wiley & Sons.

[3] Awtar, S., Quint, J., and Ustick, J., 2020, "Experimental Characterization of a Large-Range Parallel Kinematic XYZ Flexure Mechanism," Journal of Mechanisms and Robotics, **12**(6), p. 061011.

[4] Howell, L. L. and Midha, A., 1994, "A Method for the Design of Compliant Mechanisms With Small-Length Flexural Pivots," Journal of Mechanical Design, **116**(1), pp. 280–290.

[5] Howell, L. L. and Midha, A., 1995, "Parametric Deflection Approximations for End-Loaded, Large-Deflection Beams in Compliant Mechanisms," Journal of Mechanical Design, **117**(1), pp. 156–165.

[6] Su, H.-J., 2009, "A Pseudorigid-Body 3R Model for Determining Large Deflection of Cantilever Beams Subject to Tip Loads," Journal of Mechanisms and Robotics, **1**(2), p. 021008.

[7] Awtar, S., Slocum, A. H., and Sevincer, E., 2007, "Characteristics of Beam-Based Flexure Modules," Journal of Mechanical Design, **129**(6), pp. 625–639.

[8] Awtar, S. and Sen, S., 2010, "A Generalized Constraint Model for Two-Dimensional Beam Flexures: Nonlinear Load-Displacement Formulation," Journal of Mechanical Design, **132**(8), p. 081008.

[9] Ma, F., Bai, R., Chen, G., and Awtar, S., 2025, "Nonlinear Complementary Strain Energy Formulation for Planar Beam Flexures Undergoing Intermediate Deflection," Journal of Mechanical Design, **147**(8).

[10] Ma, F. and Chen, G., 2015, "Modeling Large Planar Deflections of Flexible Beams in Compliant Mechanisms Using Chained Beam-Constraint-Model1," Journal of Mechanisms and Robotics, **8**(2), p. 021018.

[11] Ma, F., Bai, R., and Chen, G., 2016, "Modeling Large Spatial Deflections of Slender Bisymmetric Beams in Compliant Mechanisms Using Chained Spatial-Beam-Constraint-Model (CSBCM)," Journal of Mechanisms and Robotics, **8**(4), p. 041011.

[12] Zhang, A. and Chen, G., 2013, "A comprehensive elliptic integral solution to the large deflection problems of thin beams in compliant mechanisms," Journal of Mechanisms and Robotics, **5**(2), p. 021006.

[13] Turkkan, O. A. and Su, H., 2017, "A general and efficient multiple segment method for kinetostatic analysis of planar compliant mechanisms," Mechanism and Machine Theory, **112**, pp. 205–217.

[14] Sorgonà, O., Cirelli, M., Giannini, O., and Verotti, M., 2025, "Comparison of flexibility models for the multibody simulation of compliant mechanisms," Multibody System Dynamics, **63**(3), pp. 453–474.

[15] Turkkan, O. A. and Su, H.-J., 2016, "DAS-2D: a concept design tool for compliant mechanisms," Mechanical Sciences, **7**(2), pp. 135–148.

[16] Su, H.-J., 2026, "Open Source Hierarchical Multi-fidelity Modeling Stack for Parallelogram Flexures," https://github.com/haijunsu-osu/parallelogram_model_comparison.

List of Figures

List of Tables